Supplementary information

Metasurface integrated high energy efficient and high linearly polarized InGaN/GaN light emitting diode

Miao Wang[1,2,3], Bing Cao[1,2,], Fuyang Xu[1,2], Linghua Chen[1,2], Yu Lin[1,2], Chinhua Wang[1,2,*], Jianfeng Wang[3], and Ke Xu[3]*

[1]*College of Physics, Optoelectronics and Energy & Collaborative Innovation Center of Suzhou Nano Science and Technology, Soochow University, Suzhou 215006, China.*

[2]*Key Lab of Advanced Optical Manufacturing Technologies of Jiangsu Province & Key Lab of Modern Optical Technologies of Education Ministry of China, Soochow University, Suzhou 215006, China.*

[3]*Suzhou Institute of Nano-tech and Nano-bionics, Chinese Academy of Sciences, Suzhou, 215125, China.*

Contents

*Corresponding authors. E-mail address: bcao2006@163.com , chinhua.wang@suda.edu.cn

1. The Finite-Difference Time-Domain (FDTD) method

The Finite-Difference Time-Domain (FDTD) method[1,2,3] is a method for solving Maxwell's equations in complex geometries. The time-dependent Maxwell's equations (in partial differential form) are discretized using central-difference approximations to the space and time partial derivatives. The resulting finite-difference equations are solved in either software or hardware in a leapfrog manner: the electric field vector components in a volume of space are solved at a given instant in time; then the magnetic field vector components in the same spatial volume are solved at the next instant in time; and the process is repeated over and over again until the desired transient or steady-state electromagnetic field behavior is fully evolved. Being a direct time and space solution, it offers the user a unique insight into all types of problems in electromagnetics and photonics. In addition, FDTD can also obtain the frequency solution by exploiting Fourier transforms, thus a full range of useful quantities can be calculated, such as the complex Poynting vector and the transmission/reflection of light. The following important attentions were paid regarding the use of FDTD method:

1.1 Materials Database

The Materials Database allows for the definition of complex materials using experimental data or parametrized models. The Material Database stores the material data to be used in the simulation. Dispersive materials with tabulated refractive index (*n, k*) data as a function of wavelength can be incorporated by using the multi-coefficient material models that automatically generates a material model based on the tabulated data. Specific models such as Drude, Debye or Lorentz can also be used.

In our simulation, the refractive index (*n, k*) of Al and Ag is calculated using Drude model, and the refractive index (*n, k*) data of GaN is measured by an ellipsometer in the wavelength range of 400-600nm, from which a material model was automatically generated and used in the FDTD. The measured refractive index (*n, k*) of GaN are given as follows:

Table S1

Wavelength (nm)	n	k	Wavelength (nm)	n	k
375.76	2.675	0	459.26	2.471	0
400.00	2.565	0	539.13	2.408	0
427.59	2.510	0	590.48	2.393	0
459.26	2.471	0	620.00	2.383	0

1.2 Boundary Conditions

The FDTD solver supports a range of boundary conditions (BCs), such as perfectly matched layer (PML), periodic, and Bloch. PML boundaries absorb electromagnetic waves incident upon them. They essentially model open (or reflectionless) boundaries. PML boundaries perform best when the surrounding structures extend completely through the boundary condition region. Periodic BCs are used when both the structures and electromagnetic (EM) fields are periodic. Periodic boundary conditions can be used in one direction, i.e. only in the X direction, to simulate a structure which is periodic in this direction but not necessarily other directions. Bloch BCs should be used when the structures and the EM fields are periodic, but a phase shift exists between each period.

In our design of Elliptic Metal Cylinder Array (EMCA), periodic boundary conditions are used at both X′ and Y′ boundaries, and PML condition is utilized at Z′ boundaries.

1.3 Meshing

The fundamental simulation quantities (material properties and geometrical information, electric and magnetic fields) are calculated at each mesh point (usually in rectangular and Cartesian style) in FDTD. A smaller mesh allows for a more accurate representation of the device, but at a substantial cost including the time and memory required. Generally, $\lambda/dx=10$ is considered reasonable for many FDTD simulations and $\lambda/dx \sim 20$ is considered very high accuracy. In some cases, it is also necessary to manually add additional meshing constraints, which involves forcing the mesh to be smaller near complex structures (often metal) where the fields are changing very rapidly, or in high index (to maintain a constant number of mesh points per wavelength) and highly absorbing (resolve penetration depths) materials.

In our simulation, the mesh accuracy was set as $\lambda/dx \sim 20$ in the overall structure. Smaller mesh (dx, dy, dz=2nm at wavelength 533nm) were added in the regions of EMCA and DMBiWG.

[1]. Dennis M. Sullivan, Electromagnetic simulation using the FDTD method. New York: *IEEE Press Series, (2000).*

[2]. Allen Taflove, Computational Electromagnetics: The Finite-Difference Time-Domain Method. *Boston: Artech House, (2005).*

[3]. Stephen D. Gedney, Introduction to the Finite-Difference Time-Domain (FDTD) Method for Electromagnetics. *Morgan & Claypool publishers, (2011).*

2. Dielectric/metal bi-layered wire grids (DMBiWG)

2.1 Optimization of H3, P and DC of DMBiWG

The effects of thickness of the transition dielectric layer (H3) of PMMA (n533nm=1.495) with lower refractive index than GaN (n530nm=2.42) and the grid period (P) on the performance of the device, i.e., TMT，TET and ER, are shown in Fig. S1 and Fig. S2, respectively. It is seen, from Fig. S1, that significant enhancement in both TMT and ER can be achieved with the introduction of a low-refractive dielectric layer over a wide range of layer thickness. The TMT and ER of the structure with an optimized dielectric layer reach 85% and 38 dB, respectively, in contrast to that less than 65% TMT and 34 dB ER of the structure without the dielectric layer (1st point in Fig. S1). The physical mechanism behind the enhancement of TMT and ER can be understood from interference phenomena within the 3-layer structure of GaN/transition layer/effective metal grating layer, and the effective medium theory of the sub-wavelength metallic nanograting. The oscillating behavior of TMT and ER in Fig. S1 clearly shows the interference effect from the 3-layer structure. Fig. S2 shows further the different behaviors of TMT and ER on the grid period with and without the transition layer (H3). When the grid period (P) is increased to 200 nm, the TMT and ER of the bare grating structure decreases to less than 20% and ~30 dB, respectively, while the TMT and ER of the structure with the transition layer remain almost flat at >80% and >35 dB, respectively. This implies that the requirement for the grating period can be significantly loosened for a fixed TMT and ER if an appropriate dielectric transition layer is introduced, which will significantly reduce the fabrication difficulty. In order to acquire a higher transmission of TM, we set the medium grating period at 150nm.

Fig. S3 shows the different behaviors of TMT and ER on the duty cycle (DC) of grid period with and without the transition layer (H3). The TMT and ER of the **DMBiWG** structure reach 85% and ~37 dB, respectively, when DC is increased to 0.5.

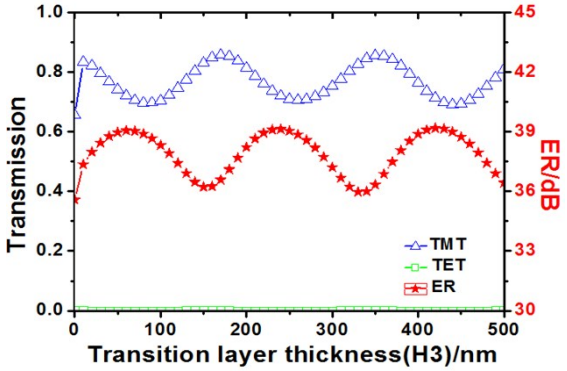

Figure.S1 Polarization properties (TMT TET and ER) versus thickness (H3) of the dielectric layer. The parameters for P=150 nm, H1=55 nm, H2=80 nm and Duty cycle DC=W/P=0.5

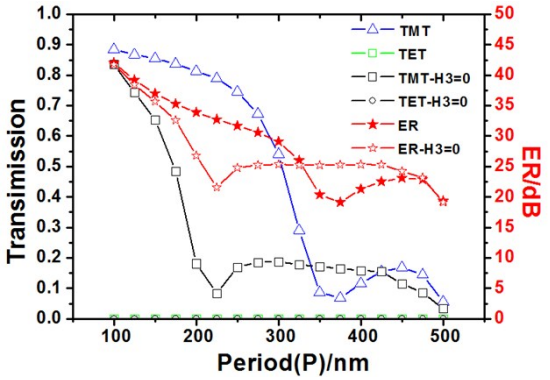

Figure.S2 Polarization properties (TMT TET and ER) versus the grating period (P). The parameters for H1=55 nm, H2=80 nm, H3=180 nm and DC=0.5.

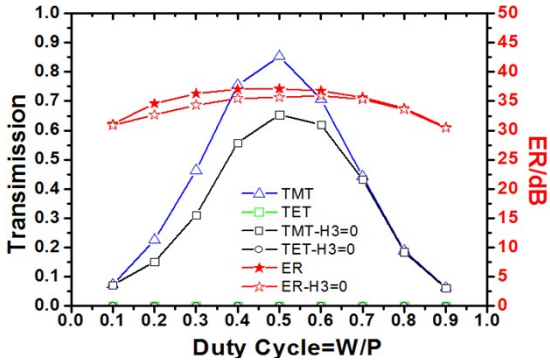

Figure.S3 Polarization properties (TMT TET and ER) versus the duty cycle (DC). The parameters for P=150 nm, H1=55 nm, H2=80 nm, H3=180 nm and DC=0.5.

2.2 Optimization of H2 and H1 of DMBiWG

Fig. S4(a) and (b) show the effect of the thickness of medium grating (H2) and the thickness of both Al grating(H1) on the polarization properties of the device. In Fig. S4(a), it is seen that both TMT and ER are sensitive to the thickness of the medium grating (H2) with an optimized value at H2~80 nm, at which TMT=85% and ER=37 dB. This resonant phenomenon of TMT and ER with the thickness of H2 can be explained by the fact that the DMBiWG structure is actually a cascaded two metal gratings separated by a medium grating, the light transmitted through the first (lower) metal grating is partially reflected by the second (upper) metal grating and it travels back and forth between the two gratings leading to constructive or destructive interference at certain separations for either TM or TE mode, which can be determined by F-P coupling effect. The performance of the structure without the transition layer, i.e., H3=0, is also shown in Fig. S4 for comparison. In Fig. S4(b), it is clear that while ER increases with the thickness of the Al grating, as expected, the TMT remains at a high value of >80% in a wide range of 20-60 nm, which is in contrast to that with H3=0.

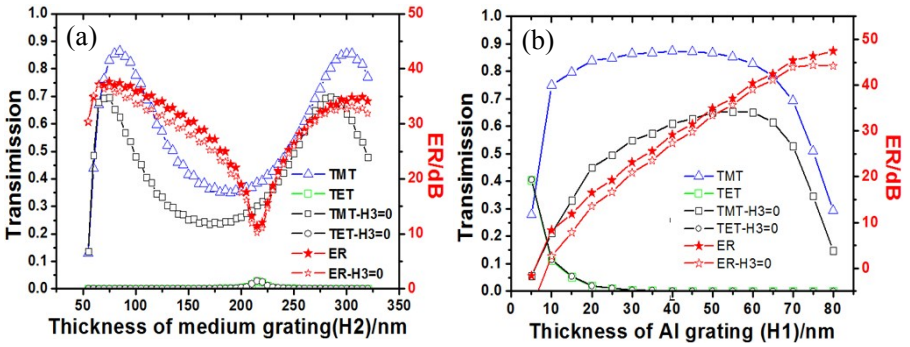

Figure.S4 TMT and ER versus (a) thickness of medium grating (H2) and (b) thickness of Al grating (H1). Parameters: P=150 nm, DC=0.5, H3=180 nm and H1=55 nm for (a), H2=80 nm for (b).

3. Elliptic Metal Cylinder Array (EMCA) Metasurface

The detailed nano-structure of an elliptic metal cylinder array (EMCA) metasurface is shown Figure S5. Elliptical metal cylinders with dimensions of short axis *a*, long axis *b* and height *T* are arranged in array with the unit cell (periods of the unit along short axis and long axis of the elliptical cylinders are P1 and P2, respectively), as shown in the dotted box of Figure S5 (left). The EMCA is a reflecting metasurface which can function as various waveplates depending on the ellipticity and height of the cylinders. The characteristics of the EMCA metasurface is designed and calculated

using FDTD method. To design and simulate the performance of an EMCA structure, X′Y′Z′ coordinates and relative orientation of the structural elements is defined and shown in Figure S5 (left). Periodic boundary conditions are used at the X′ and Y′ boundaries, and perfectly matched layers condition is utilized at the Z′ boundaries in the simulation. The incident field is assumed to be a linearly polarized along the direction of 45° with respect to X′ and Y′ axis conforming to typical application orientation of conventional bulk waveplates.

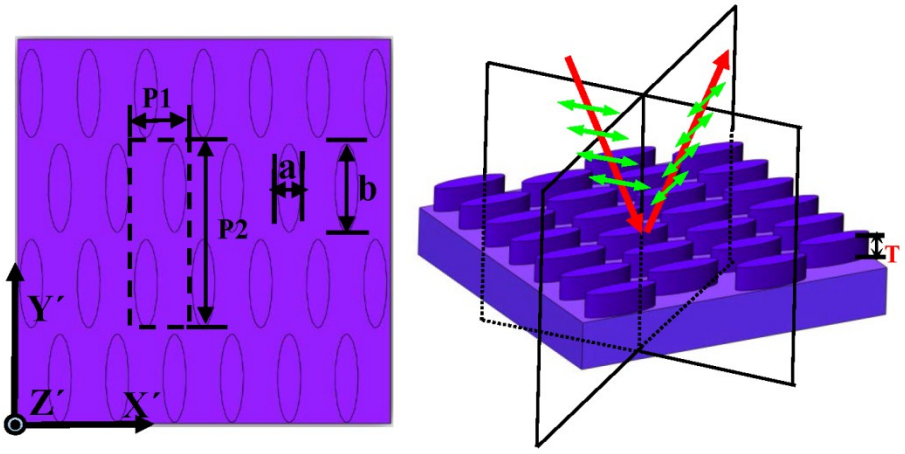

Figure S5: Diagram of an elliptical metal (Ag) cylinder array (EMCA) metasurface structure

3.1 Optimization of long axis (b) of elliptic cylinder of an EMCA

The short axis *a* is fixed at 110nm, the long axis *b* is optimized. Other parameters are P1=280nm, P2=850nm, T=105nm. It is seen, from Figure S6, that high reflectivity(>80%) and large phase difference (>π) between two perpendicular directions of X′and Y' axis can be obtained within the spectral range of green light. The inset of Figure S6 shows that diagram of the EMCA metasurface when the value of long axis changes while short axis remains at 110nm. It is seen that the phase difference can be manipulated by the ratio of long axis and short axis (*b/a*). As expected, when long axis is equal to short axis, the phase difference is almost zero. When long axis is larger than 330nm, i.e., *b/a* is larger than 3, the sensitivity of the phase difference on the ratio *b/a* becomes flat. Detailed examination shows that the optimized ratio of *b/a* for a π phase shift is *b*=400nm at 530nm.

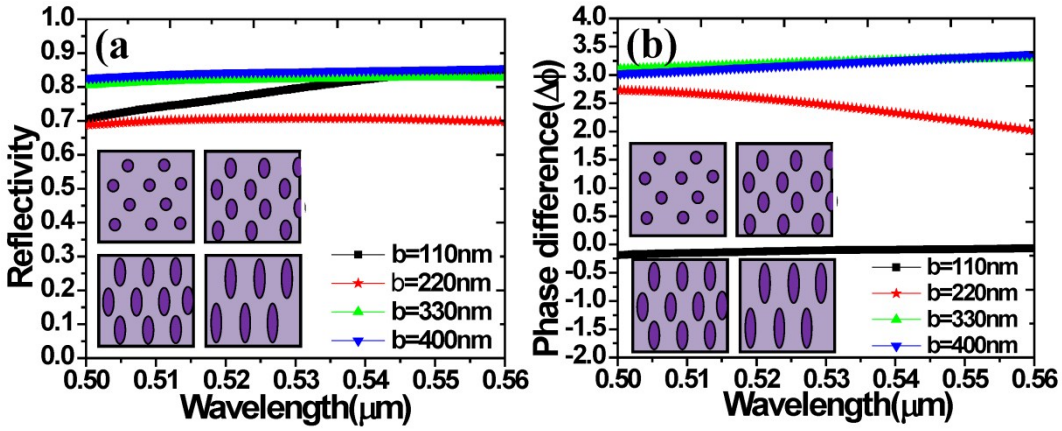

Figure S6: Wavelength dependent reflectivity (left) and phase difference (right) of a silver EMCA metasurface with varying long axis *b*. Parameters: *a*=110nm, P1=280nm, P2=850nm, T=105nm.

3.2 Optimization of elliptic cylinder height (T) of an EMCA

The height (T) of elliptic cylinder of the EMCA is optimized when the elliptic short and long axis are chosen at *a*=110nm, *b*=400nm, and P1=280nm, P2=850nm.

Figure S3 shows the reflectivity, amplitude and phase difference simulation results with different heights of elliptic cylinder. By manipulating the height of EMCA, the phase difference around π can be obtained. When the height of EMCA (T) changes from 95 nm to 115 nm, the amplitude of the two orthogonal reflected electric field components is approximately equal and the corresponding reflectivity reaches 85%. The range of height T that corresponds to the phase difference variation of less than 5% of π is between 100 nm and 115 nm, at 533 nm wavelength, as shown in Figure S7 (right-bottom).

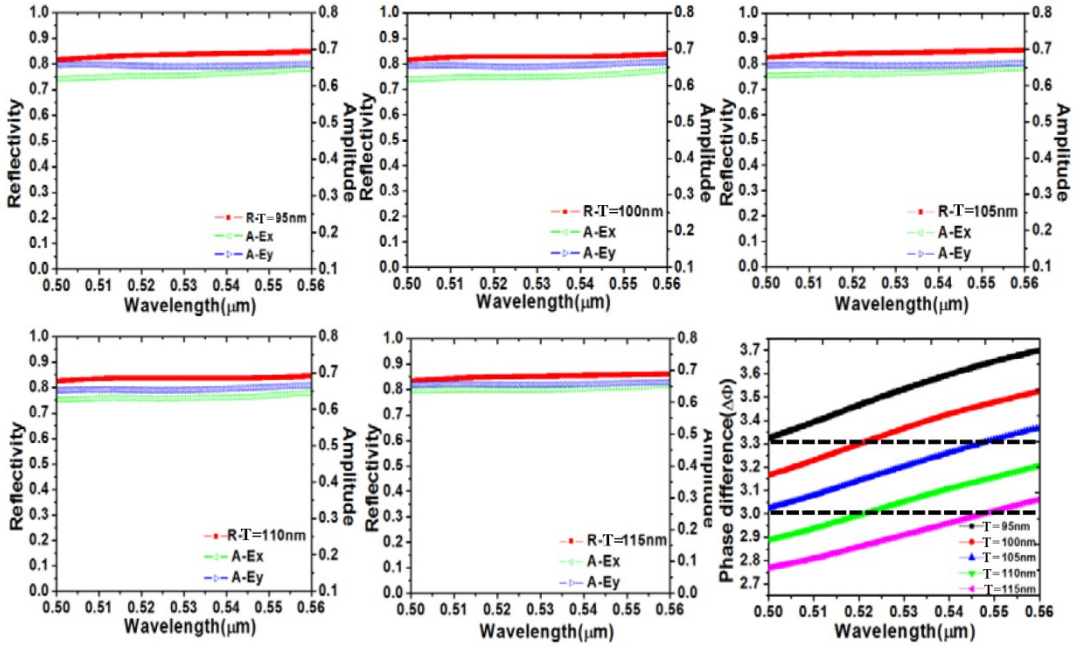

Figure S7: Simulation results of reflectivity, amplitude and phase difference with different heights of elliptic cylinder.

4. Experimental Results and Discussions

4.1 Experimental characterization of the fabricated EMCA

The fabricated EMCA was separately characterized before it is integrated with the LED. The following experiments were performed:

Firstly, the direct measurement of the polarization state of a linear polarization incident light after reflection from the fabricated EMCA was performed. It is seen from Figure S8 that the polarization state of the reflected light from the fabricated EMCA is close to that after reflection from an ideal EMCA, i.e., the major component of the reflected elliptical polarization (ellipticity and azimuth angle are 0.198 and -40.5^0, respectively, compared to 0 and -45^0 from an ideal EMCA) pointing to the perpendicular direction (ideal direction) of the incident linear polarization.

In Figure S8, the simulated polarization state of a linear polarized incident light (at wavelength 533 nm) after reflection from the fabricated EMCA using the experimentally measured dimensions of the EMCA-structure is also given for validation. The experimentally measured dimensions of the fabricated EMCA are: long axis=290 nm, short axis=120 nm, period along X′ axis (P1)=250nm, and period along Y′ axis (P2)= 850 nm, respectively, as given in the manuscript. Based on the measured dimensions of the fabricated EMCA, the amplitude ratio (i.e., Ey′/Ex′) and phase

difference (ψ) can be calculated with FDTD, in which Ey′/Ex′=0.987 and ψ=2.78 are obtained at wavelength 533 nm. The corresponding polarization state can thus be obtained according to Eq. 2 in the manuscript, in which the ellipticity and azimuth angle are 0.185 and -44.6^0, respectively. It is seen from Figure S8 that the directly measured polarization state (ellipticity and azimuth are 0.198 and -40.5^0, respectively) is consistent with the simulated polarization state (ellipticity and azimuth are 0.185 and -44.6^0, respectively) which uses the measured dimensions from the fabricated EMCA.

Based on the direct measurement of the polarization state of a linear polarization incident light after reflection from the fabricated EMCA and the simulated polarization state using the experimentally measured dimensions from the fabricated EMCA, it is confirmed that the polarization state of a linear polarization incident light after reflection from the fabricated EMCA is indeed an elliptical polarization with an ellipticity and azimuth angle being ~0.185 to 0.198 and $\sim-40.5^0$ to -44.6^0, respectively, which are very close to the ellipticity=0 and azimuth=-45^0 if reflected from an ideal EMCA.

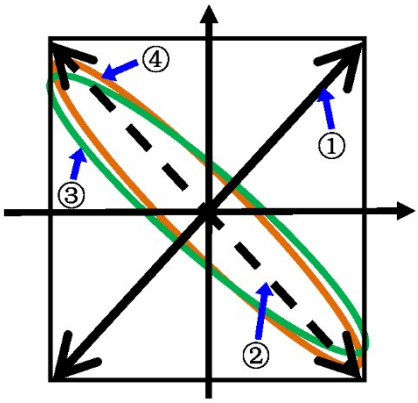

Figure S8 Experimentally measured polarization state of a linear polarized incident light after reflection from the fabricated EMCA. ①: polarization orientation of the incident linear polarization; ②: polarization orientation of the reflection from an ideal EMCA；③：Experimentally measured polarization state after reflection from the fabricated EMCA；④：Simulated polarization state after reflection from the fabricated EMCA using experimentally measured dimensions of the EMCA.

4.2 Comparison of various surface components on performance of integrated LED

(1) We have performed detailed experimental investigations and comparisons on the performance (energy extraction efficiency and extinction ratio of linear polarization output) of a LED emission by using various surface components bonded to the bottom of a LED, which includes: (1) a rough glass with a 150nm Ag deposition; (2) thick and uniform Al film on a glass substrate; (3) a fabricated quasi-circles Ag arrays pattern (Figure S9) with an Ag thickness of 110nm; and (4) a fabricated EMCA with dimensions shown in the manuscript. In this case, three measurements in which the angles between the direction of gratings and the long axis of elliptic cylinder in EMCA at 0^o , 45^o and 90^o, respectively, are conducted, and the measured results are denoted as EMCA (0^o), EMCA (45^o) and EMCA (90^o), respectively.

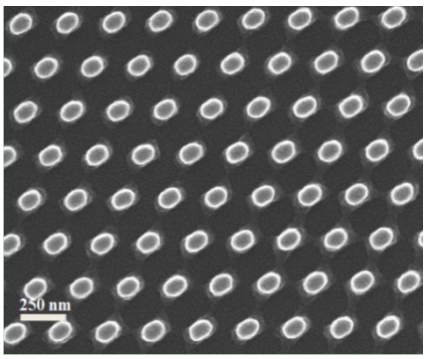

Figure S9 SEM of a fabricated Ag coated quasi-circles arrays. Long axis=70 nm and short axis=50 nm.

Table S2 shows the results of the surface reflection (from both simulation and experiment, at 533nm) of various components (before integrated to LED), including rough glass, uniform Al film, quasi-circles (shown in Figure S5), and EMCA (0^o), EMCA (45^o) and EMCA (90^o), and the corresponding energy extraction efficiency and linear extinction ratio (ER) after the integration of these components to a LED.

Table S2

	Reflection from the surface (Simulation)	Reflection from the surface (Experiment)	Energy extraction efficiency of the LED emission (compared with naked Sapphire case) (Experiment)	Linear extinction ratio(ER) of the LED emission (Experiment)
Rough Glass		＜30%	1.11	24.1 dB
Quasi-circles	79.6%	74.2%	1.14	23.7 dB
Uniform film	91.5%	86.1%	1.23	24.1dB
EMCA(0^{o})	87.5%	81.1%	1.16	23.8 dB
EMCA(45^{o})	82.6%	76.5 %	**1.44**	23.7 dB
EMCA(90^{o})	77.5%	71.9%	1.10	23.4 dB

From Table S2, we can see that:

1. The linear extinction ratio (ER) of the four structures is almost the same, which is similar to that observed in Fig. 7 in the manuscript in that the ER of the LED device is essentially determined by the upper DMBiWG polarizer.
2. The energy extraction efficiency in the case of the uniform Al mirror is higher than that of the rough glass or quasi-circles, which suggests that the energy extraction efficiency of the linear polarized emission of the LED is simply proportional to the surface reflection if there is no TE to TM polarization conversion, such as rough glass (random) or un-optimized patterned Ag quasi-circle array.
3. The energy extraction efficiency in the case of the uniform Al mirror is higher than that of EMCA(0^{o}) and EMCA(90^{o}), which suggests that the energy extraction efficiency of the linear polarized emission of the LED is proportional to the surface reflection if there is no or very small TE to TM polarization conversion. Based on this proportionality, it can be inferred that the energy extraction efficiency of the EMCA(45^{o}) should be in the range between 1.10 and 1.16 as shown in **Table S2**. However, the energy extraction efficiency of the EMCA(45^{o}) we measured is 1.44, which provides solid evidence that the improvement of 28% from the EMCA(0^{o}) or 34% from the EMCA(90^{o}) is actually due to the polarization conversion. The energy extraction efficiency of the fabricated EMCA is the highest among the four structures although the reflection of the EMCA is lower than that of the Al-coated

one, which again proves that the improvement of 21% in energy extraction efficiency from the Al mirror is actually from the polarization conversion of the optimized EMCA structure.

4. To further illustrate the mechanism behind the improvement of the energy extraction efficiency of using EMCA structure, Table S3 gives both theoretical and experimental results of the reflected polarization states (ellipticity and azimuth angle) of a linear polarization incidence (incident polarization azimuth angle is 45^o with respect to X axis) from the four different surfaces (before integrated to LED). It is seen that the azimuth angle of the reflected polarization from rough glass, Al film and quasi-circles is essentially the same as that of the incident linear polarization (i.e., 45^o). In contrast, the azimuth angle of the reflection from the EMCA surface changes to -40.5^0(experiments), which is rotated about 95.5^o with respect to the incident polarization. This rotation (conversion) of the polarization state after reflection from the EMCA is the fundamental mechanism behind the improvement of the energy extraction efficiency of using an EMCA structure.

Table S3

	Ellipticity (Theory)	Ellipticity (Exp.)	Azimuth (Theory)	Azimuth (Exp.)
Rough Glass		0.019		37.3^o
Al Film	0	0.011	45.0^o	44.6^o
Quasi-circles	0.086	0.096	43.4^o	41.4^o
EMCA(45^o)	0.185	0.198	-44.6^o	-40.5^o

5. To visualize the polarization conversion in Table S3, Figure S10 shows the polarization states of a linearly polarized incidence after reflection from the EMCA surface and the quasi-circles arrays at 533nm wavelength. The black dashed line in Figure S6 corresponds to a perfect performance of an EMCA half waveplate in which the reflection polarization is rotated by exactly 90^o from the incidence. In the case of EMCA surface, the major component of the reflected elliptical polarization is also rotated by approximately 90^o from the incidence. In contrast, the reflected polarization from the quasi-circles changes only 3.6^o from the incident polarization.

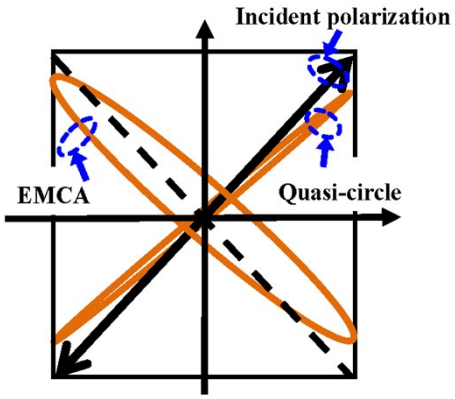

Figure S10 Polarization states of a linearly polarized incidence after reflection from the fabricated EMCA and the fabricated quasi-circles surfaces at 533nm wavelength.

4.3 Discussions on the improved energy extraction efficiency

If no optical absorption and no optical losses are considered in GaN and especially in quantum well (QW), the FDTD simulated value of efficiency gain of an ideal EMCA device is about 175% higher than the Al-coated one, which is understandable, because all the TE components that are otherwise wasted in the case of Al-mirror are transformed into TM components and emit out of the structure after considering a transmission of ~80% through top DMBiWG polarizer and a reflection of ~80% from EMCA surface.

In the experimental results, the improvement of the flat-Al mirror was measured to be 20% higher than the naked sapphire case, which means that nearly 80% of energy is lost when the light passes through the integrated structure, especially the QW structure. Based on this value, the efficiency gain of an ideal EMCA device is reduced to 175%×20%=35% versus the Al-coated one. In our experiment, a 20% efficiency gain based on the fabricated EMCA was measured when compared with that of an Al-coated one, which is quite reasonable when considering the deviations between the dimensions, shape and roughness, etc. of the fabricated structure and the theoretical geometries in simulation.

4.4 Thermal analysis of bonding of extra EMCA layer on the sapphire substrate

At the present device structure in which the EMCA layer is bonded to the sapphire substrate, the

temperature of the device will be increased. We have made a quantitative analysis and comparison on the thermal analysis of the proposed device and a conventional device using ANSYS software.

In the simulation, the size of the chip we simulated is 300um×300um， and the power of chip is 0.3W. The thermal conductivity of the optical adhesive we used is 0.81W/m·K. The temperature of the heat dissipation substrate is fixed at 25℃.

Figure S11 (a) shows a standard structure of LED chip which is welded on a heat dissipation substrate (AlN) by Au/Sn. **Figure S11** (b) is the proposed device structure in which a layer of optical adhesive (~3um, extra source of the thermal resistance) is added onto a sapphire substrate.

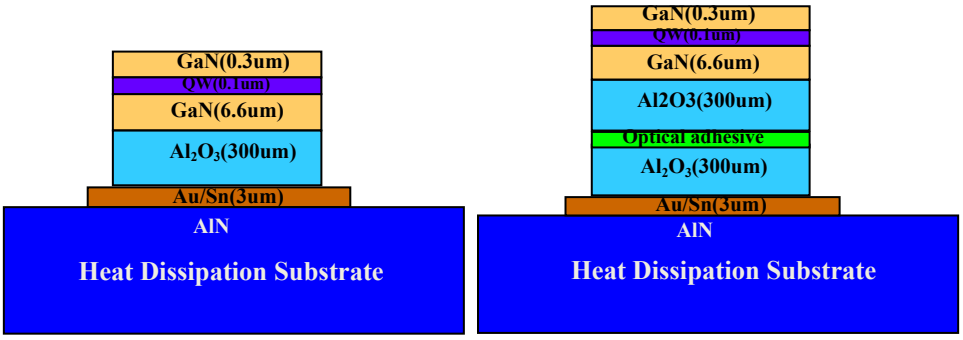

(a) (b)

Figure S11 Thermal analysis of the proposed device structure

Figure S12 (a) and (b) show the thermal distribution of device in steady state. It is seen that the temperature of the chip rises about 30℃ because of adding a layer of optical adhesive. Although the calculated absolute temperature of the proposed device is not critical for operating, the issue of the temperature increase when compared with that of a conventional device should better be addressed from the point of view of practical applications. One of the possible ways is that EMCA structure can be directly fabricated onto the Al_2O_3 substrate of the device so that an extra EMCA on a substrate and the bonding adhesive glue can be avoided. In this way, the thermal issues related to the bonding glue can be completely eliminated. In this manuscript, the main purpose is to verify the mechanism and the feasibility of the device, the thermal issues will be investigated further in the following work.

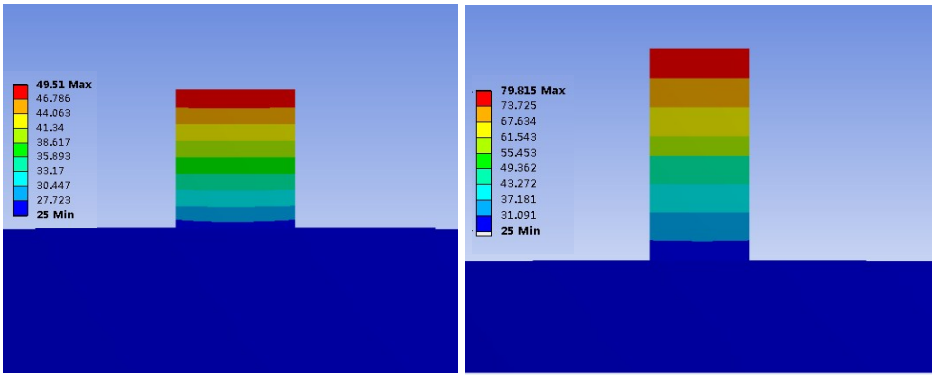

(a) (b)

Figure S12 Thermal distribution of device in steady state